

Temperature-independent curvature sensor based on in-fiber Mach-Zehnder interferometer using hollow-core fiber

S. Marrujo-García, I. Hernández-Romano, M. Torres-Cisneros, D. A. May-Arrijoja, Vladimir P. Minkovich, *Member, IEEE*, D. Monzón-Hernández, *Member, IEEE*

Abstract—An in-fiber Mach-Zehnder Interferometer (MZI), based on hollow core fiber (HCF), for measuring curvature is fabricated and experimentally demonstrated. The sensing part was fabricated by splicing a section of HCF between two sections of multimode fiber (MMF), and different HCF lengths were investigated in order to achieve the highest curvature sensitivity. These devices were tested in a transmission configuration using lead-in and lead-out single mode fibers (SMF). The sensor was attached to a steel sheet by using the polymer Polydimethylsiloxane (PDMS) for accurate control of the applied curvature. The modal analysis was carried out using a commercial software based on finite element method (FEM) and, by incorporating some of the experimental data, it was feasible to determine the two dominant modes that interfere in this sensor. The devices were characterized by measuring the fringe contrast variations due to the curvature changes. The interferometer fabricated with a HCF 2.5 mm in length HCF showed the highest curvature sensitivity, -17.28 ± 2.30 dB/m⁻¹, in a range from 1.84 m⁻¹ to 2.94 m⁻¹. Moreover, the sensor that exhibited a better performance was fabricated with a HCF length of 1 mm, combining the most extensive curvature range (from 0.95 m⁻¹ to 2.68 m⁻¹) and an adequate sensitivity (-11.80 ± 1.30 dB/m⁻¹). The analysis of the interferometric signal of this device in Fourier domain, allows us to establish a one to one relationship between the contrast and the curvature in a broader range (from 0 m⁻¹ to 2.94 m⁻¹). Moreover, the fringe contrast showed a very low dependency on temperature (from 30°C to 90 °C), showing that this device was not affected by temperate fluctuation.

Index Terms—Curvature measurement, Mach-Zehnder interferometer, Hollow core fiber, fiber optic sensor.

I. INTRODUCTION

FOR several years fiber optic sensors have been widely investigated, and this great effort has generated well-established technology and commercial devices. These

sensors offer excellent features such as small size, low-cost fabrication, lightweight, immunity to electromagnetic interference, and resistance to harsh environments. All these favorable characteristics make them attractive for developing sensors capable of measuring different variables such as temperature [1], refractive index [2], pressure [3], strain [4], and curvature [4]. Curvature is a crucial parameter in the industry with countless applications in areas like mechanical engineering [5], structural engineering [6], and also robotic arms [7] that require constant monitoring systems for measuring bending deformation. Fiber optic bending sensors have been an excellent option to address that issue, so far, various schemes based on fiber Bragg gratings (FBG) [8], long period fiber grating (LPFG) [9], modal interference [10, 11, 12], and Mach-Zehnder Interferometers (MZI) [4, 13, 14, 15] (using different specialty fibers or unusual splicing techniques) have been used. It is worthwhile noting that there are two critical parameters in a fiber bending sensor, sensitivity and curvature range, that should be considered before using them in an application. For instance, Y. Zhang et al. [8] demonstrated a sensor based on a FBG, which was engraved in central core of a seven-core fiber, it exhibited a curvature sensitivity and curvature measurement range of -7.27 dB/m⁻¹ and from 0 m⁻¹ to 1 m⁻¹, respectively. FBG was also inscribed in an abrupt biconical taper [16], in this case the constrast was monitoring, showing a maximum sensitivity of 0.1196 dB/m⁻¹ (from 0 to 80 m⁻¹). Besides, a curvature sensor that was fabricated by two LPFGs (separated by a small segment of MMF) was demonstrated [17] and its maximum sensitivity was -21.080 nm/m⁻¹ (from 0.246 to 0.738 m⁻¹). Moreover, Y. Zhao et al. [10] demonstrated a fiber optic bending sensor based on modal interference that used 5 cm of HCF sandwiched between two segments of SMF; the splice sections were made by an abrupt

I. Hernández-Romano is with the CONACYT-Electronics Department, DICIS, University of Guanajuato, Guanajuato 36885, México (e-mail: hrmano@ugto.mx)

D. A. May-Arrijoja is with the Fiber and Integrated Optics Laboratory (FIOLab), Centro de Investigaciones en Optica A.C., Aguascalientes, México (e-mail: darrijoja@cio.mx).

V. P. Minkovich and D. Monzon-Hernandez, are with the Centro de Investigaciones en Óptica A.C., León 37150, México (e-mail: vladimir@cio.mx; dmonzon@cio.mx).

This work was supported by the Consejo Nacional de Ciencia y Tecnología (CONACYT) from Mexico under the CIENCIA BÁSICA Project number No. CB2016-286368, (CB2016-286629) and Universidad de Guanajuato (UGTO) scholarship. (Corresponding author: Iván Hernández-

S. Marrujo-García and Torres-Cisneros are with the Electronics Department, DICIS, University of Guanajuato, Guanajuato 36885, México (e-mail: s.marrujogarcia@ugto.mx, nge_smg1@hotmail.com; torres.cisneros@ugto.mx).

taper. This device shows a curvature measurement range from 0.765 m^{-1} to 3.423 m^{-1} and a curvature sensitivity of (5.05 dB/m^{-1}) . The sensor proposed by Y. Gong et al. [11], based on modal interference, has a good curvature sensitivity $-130.37 \text{ dB/m}^{-1}$, but a very narrow curvature dynamic range (from 0.11 m^{-1} to 0.34 m^{-1}). On the other hand, a MZI was implemented by inserting a segment of hollow annular core fiber between two sections of MMF [13], Y. Zhang et al. report a nonlinear response in the whole interval (from 0.55 to 5.405 m^{-1}). Additionally, bending sensors based on anti-resonant reflecting optical waveguide have been implemented; S. Wang et al. [18] fabricated sensor whose curvature sensitivity was -15.33 dB/m^{-1} , and the curvature range starts from 0 m^{-1} to 1 m^{-1} , respectively. H. Cheng et al. [19] proposed a sensor that was capable of measuring curvature and temperature, their sensitivities were -4.28 dB/m^{-1} (from 10.72 m^{-1} to 11.60 m^{-1}) and $25.76 \text{ pm}/^\circ\text{C}$, respectively. R. Gao et al. [20] fabricated one-dimensional vector bending sensor by infiltrating two symmetric air holes in a hollow-core PCF, its sensitivities (for two apposite directions) were 4.86 and -4.84 dB/m^{-1} (from 0 to 0.88 m^{-1}). However, most of the previous studies did not show the possibility of choosing different curvature range or sensitivity by means of modifying the structure of the fiber sensor. Therefore, their industrial application might be limited to specific problems where high sensibility or wide curvature range is needed. Additionally, all of them require either expensive materials or equipment due to complex fabrication techniques.

Here, we propose, simulate, and experimentally demonstrate an in-fiber MZI sensor for measuring curvature. The sensor was fabricated by splicing a section of HCF between two sections of MMF. The device was attached to a steel sheet with the aid of PDMS to ensure that the bending direction was confined to one plane. Covering the device with polymer makes it sturdy (creating a package for real application) and opens the possibility to be attached to any surface, without modifying the sensor response according to our experimental results. Different sensors were fabricated by changing the length of the HCF, and they were characterized by measuring changes of the fringe contrast as a function of the induced curvature. The interferometer fabricated with a HCF length of 2.5 mm showed the highest curvature sensitivity, $-17.28 \pm 2.30 \text{ dB/m}^{-1}$, in a range from 1.84 m^{-1} to 2.94 m^{-1} . By simply modifying the HCF length to 1 mm , a device that exhibited an optimum performance can be easily obtained, i.e., a sensor with an adequate sensitivity and curvature measurement range. Its curvature sensitivity was $-11.80 \pm 1.30 \text{ dB/m}^{-1}$, in a range from 0.95 m^{-1} to 2.68 m^{-1} . The output signal of this sensor was Fourier-transformed, and the analysis shows that a one to one relationship exists between the contrast and the curvature without ambiguity in a wider range (from 0 m^{-1} to 2.94 m^{-1}). The Trial Version of the image contrast did not change during a temperature test (from 30°C to 90°C), showing that this device was not affected by temperate fluctuation.

II. FABRICATION PROCESS AND WORKING PRINCIPLE

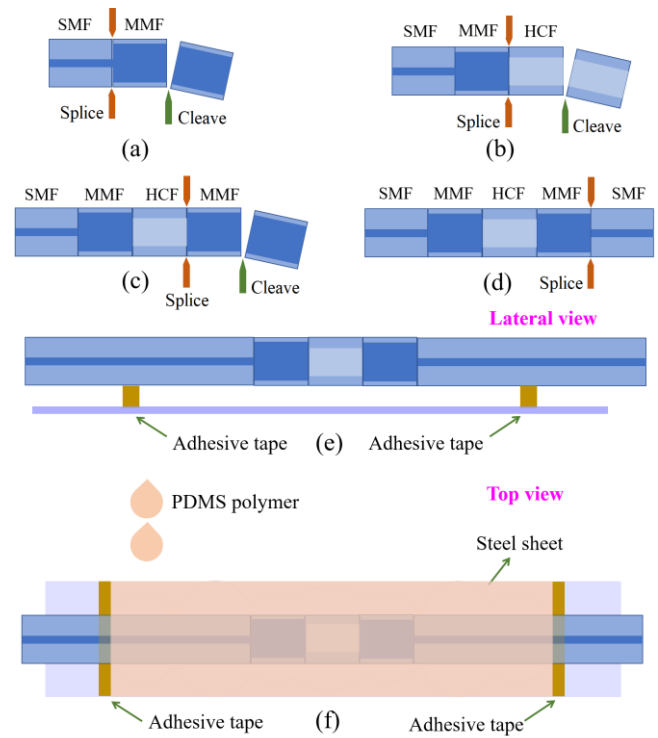


Fig. 1. Fabrication process: (a)-(d) Cutting and splicing the elements that form the sensor, (e) Mounting the sensor over the steel sheet (f) Covering the sensor with a polymer.

All the structures in this work are fabricated by using SMF ($9/125 \mu\text{m}$), MMF ($105/125 \mu\text{m}$), and HCF (inner and outer diameters are 65.5 and $125 \mu\text{m}$, respectively). The MZIs were fabricated by sandwiching different lengths of HCFs between two sections of MMF, and this structure was spliced between lead-in and lead-out SMFs, see Fig. 1 (a)-(d). The length of the two MMFs was 1 mm , and these fiber sections worked as a mode coupler. Six different lengths (0.5 , 1 , 1.5 , 2 , 2.5 , and 3 mm) of HCF were used to assembly the MZIs. A special program for splicing MMF and HCF was developed using a Fitel splicer (model s179), which allows us to reduce insertion losses due to the splicing between dissimilar fibers. Each sensor was mounted on a flexible steel sheet by holding it straight over the steel sheet with the aid of small pieces of adhesive tape, see Fig. 1 (e). It is worth mentioning that the fiber optic sensor and the whole fiber never got in contact with the steel sheet. Finally, the device was permanently attached in the middle of the 31 cm long steel sheet with the aid of PDMS polymer, with a length of 13 cm covered with PDMS, see Fig. 1 (f). The polymer was cured following the manufacture's specifications. As previously mentioned, by attaching the sensor to a steel sheet, we guarantee that the bending direction was performed in one plane, without torsion effects, which allows us to characterize the sensor under controlled bending conditions. Moreover, during the design of the package of this sensor, we considered the position of the optical fiber inside the polymer to avoid any strain suffered by the device. For example, W. H. PNG et al. fabricated a bending sensor using

a tapered fiber embedded in a polymer and this device was glued on a steel bar. The authors said that there is a neutral axis inside along this package, it is defined as the axis that does not experience any elongation (remains at the same length) when the segment is imposed to be bent [6]. They took advantage of this strain and set the tapered fiber out of the neutral axis. In our case, we do not want that the sensor suffers any strain due to the polymer, then, the device was set in the neutral axis (in the middle of the polymer), see Fig. 2. The thickness of the polymer was 4 mm.

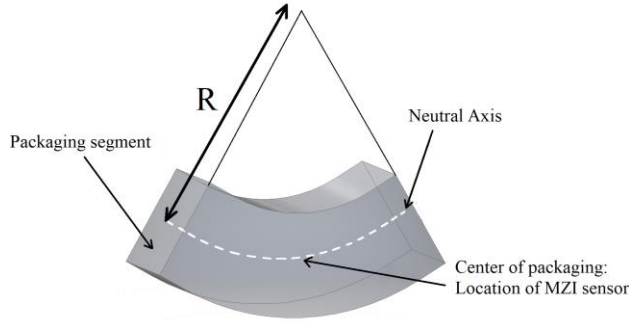


Fig. 2. Schematic drawing that shows the position of the optical fiber inside the polymer (sensor packaging).

The experimental setup implemented to test the different MZIs is shown in Fig. 3. The Superluminescent Diode (SLD-1550S-A40, Thorlabs), centered at 1550 nm, was used as a broadband source to launch light into the MZIs. The output spectrum of the device was measured employing an Optical Spectrum Analyzer (OSA) (MS9740A, Anritsu).

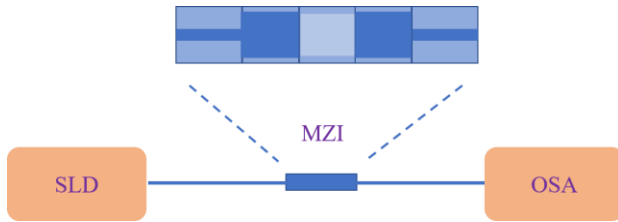


Fig. 3. Experimental setup to test the transmission of MZIs.

Before performing any characterization, we evaluated the impact of the PDMS on the spectral response of the HCF sensor. This task is realized by fabricating a MZI with a HCF length of 1 mm, attaching it to the steel sheet with the adhesive tape, and taking its spectral response. Afterward, we cover the sensor with PDMS, cure it, and retake its spectrum. As shown in Fig. 4, the phase and maximum contrast differences are 0.08 nm and 0.57 dB, respectively. There are no significant changes in these two signals.

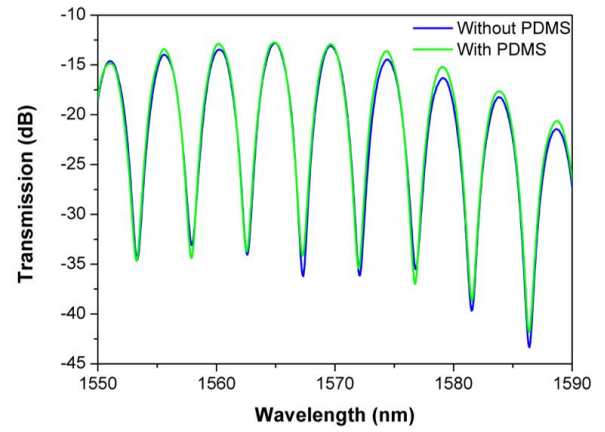


Fig. 4. Experimental spectrum of MZI sensors with a HCF length of 1 mm, with PDMS and without PDMS.

The transmission spectrum of this fiber device can be expressed by the following equation [21]

$$I = I_{ch} + I_{rclad} + 2\sqrt{I_{ch}I_{rclad}}\cos\left\{\frac{2\pi\Delta n_{eff}}{\lambda}L\right\}, \quad (1)$$

where $\Delta n_{eff} = n_{ch,eff} - n_{rclad,eff}$. I_{ch} and I_{rclad} are the intensities of the propagated beams in the central hole and in the ring-cladding, respectively; Δn_{eff} , $n_{ch,eff}$, and $n_{rclad,eff}$ are the effective refractive index difference (ERID), the effective refractive index (ERI) of the central hole, and the ERI of the ring-cladding, respectively. L and λ are the length of the HCF and the wavelength of the light, respectively.

In Ref. [21], it was also shown that a linear relationship exists between the spatial frequency (ξ) and the length L ,

$$\xi = \frac{1}{\lambda^2}\Delta n_{eff}L, \quad (2)$$

where the spatial frequency is the number of cycles per nm. Therefore, Eq. (2) can be used to determine Δn_{eff} by using different lengths (L) of HCF [21]. Knowing this value, it is feasible to simulate the spectrum of this MZI for future applications as well as to find out the modes that interfere.

Fig. 5. (a) shows the interferometric signal of the MZIs constructed with different HCF lengths (0.5, 1, 1.5, 2, 2.5, and 3 mm). The device fabricated with a HCF length of 0.5 mm showed the highest contrast (30.40 dB), and its FSR was 11.18 nm. The MZI fabricated with a HCF length of 3 mm exhibited the lowest contrast (14.80 dB), and its FSR was 1.74 nm. The spatial frequency of each MZI can be obtained by applying the Fast Fourier Transform (FFT) to the output signals, see Fig. 5 (b). It should be mention that for each HCF length three sensors were fabricated. Sensors fabricated with HCF from 1 to 3 mm exhibit a standard deviation less than 4 %, whereas the sensor fabricated with 0.5 mm shows a standard deviation of 9.4 %. It is worth mentioning that the reproducibility of the fabrication of this devices depend on length, lower reproducibility was found in shorter lengths. The experimental data and the error bar are shown in Fig. 5 (c). Plotting the spatial frequencies versus the lengths of the

HCF helps us to know the slope (ξ/L), with a value of 0.196 ± 0.007 (nm)⁻¹/mm, see Fig. 5 (c). It is possible to evaluate Δn_{eff} by using this slope, the central frequency of the spectrum (1570 nm, see Fig. 4 (a)), and the Eq. (2), which results in a $\Delta n_{eff} = 0.468 \pm 0.017$.

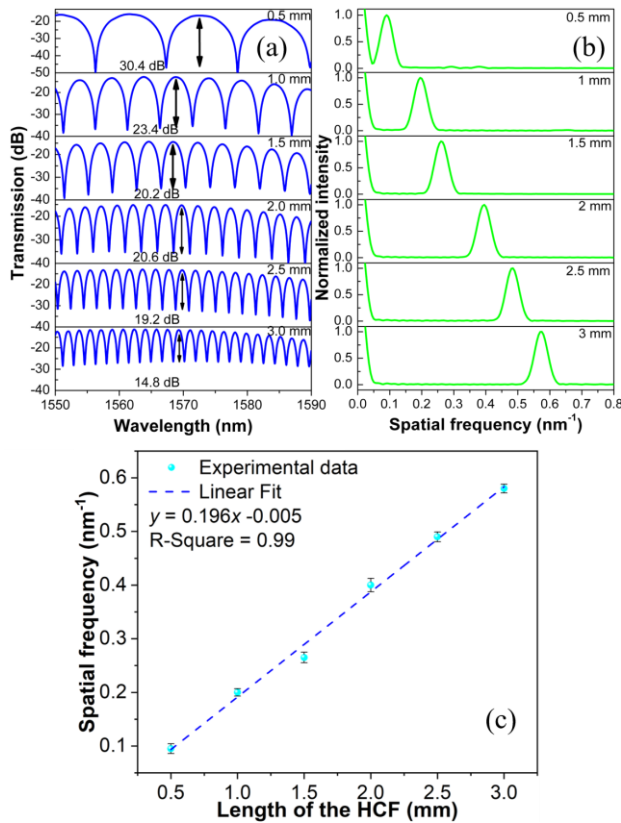


Fig. 5. Six MZIs were fabricated with different lengths of HCF (a) Transmission spectra (b) FFT of the transmission spectra. (c) Variation of the spatial frequency as a function of the HCF length.

In Fig. 5 (b), the intensity at zero spatial frequency is associated with the fundamental mode, and the other predominant peak is linked to a specific mode among the cladding modes. Other peaks are present, but their amplitudes are insignificant compared with the dominant peaks intensity. The beating between these two modes generates the interferometric pattern, and since the envelope

of this pattern does not show any modulation, this demonstrates that just two modes interfere in the MZI.

A commercial full-vector mode solver based on the finite-element method (FEM), COMSOL Multiphysics software, was used to simulate the transversal section of the HCF to calculate the ERI of the modes. In this case, for leaky-mode analysis, a strong boundary condition is required. An anisotropic perfectly matched layer (PML) was used around the cladding since the effectiveness of the PMLs has been confirmed to provide reflectionless absorption of the incident fields. The refractive indices of the PDMS and silica were calculated using the Sellmeier equation [22, 23]. With this assumptions, the fundamental mode LP₀₁ (HE_{11}^x and HE_{11}^y) was simulated [24], as shown in Fig. 6 (a), which results in a value of $n_{ch,eff} = 1.000$. It was shown in Ref. [25] that only LP_{0n} can be excited and transmitted in the HCF. Therefore, among the different modes that can propagate in the cladding, the mode shown in Fig. 6 (b) was selected to fulfill the experimental condition $\Delta n_{eff} = 0.468$; which corresponds to a value of $n_{ch,eff} = 1.444$. Using this ERI, a value of $\Delta n_{eff} = 0.444$ was calculated, it is 5 % less than the experimental value. It should be noted that this structure, where two predominant modes interfere, is very similar to the microfiber interferometer [26], where two modes are excited (HE_{11} and HE_{12}). The main difference is that the microfiber interferometer requires a tapering machine to be constructed, whereas the structure presented here is fabricated with a simple splicing machine.

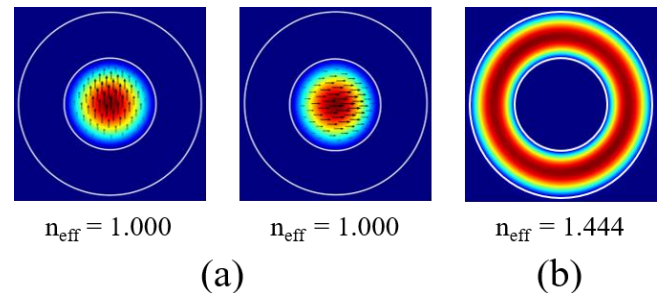


Fig. 6. Mode field distribution at (a) The center of the HCF (b) In the ring cladding.

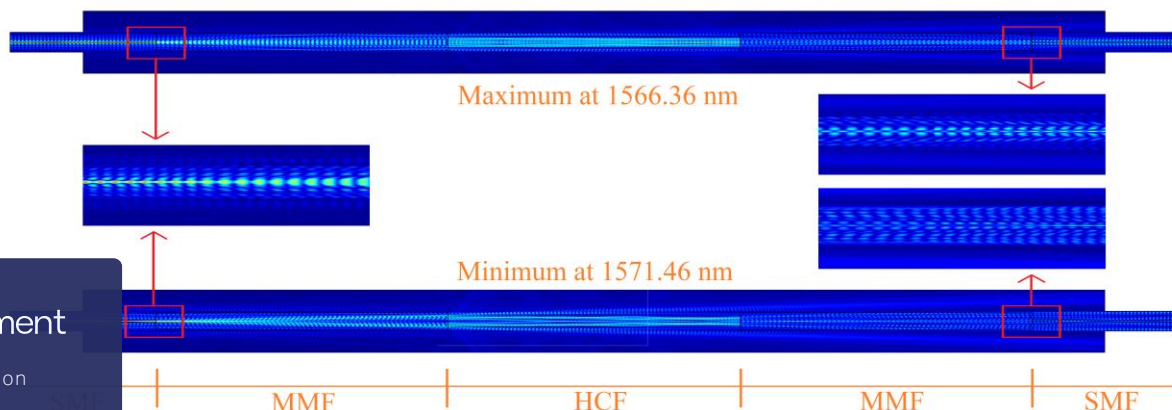


Fig. 7. FEM simulation of the electric field distribution along the MZI with 1 mm-length HCF. The wavelengths (corresponding to a maximum and a minimum) were obtained from the experimental data.

The FEM commercial software used previously was also used to simulate the electric field distribution along the MZI when it was covered with PDMS polymer. In all simulations, the beam propagation direction is the z-axis. As previously mentioned, SMF (9/125 μm), MMF (105/125 μm), and HCF (inner and outer diameters are 65.5 and 125 μm , respectively) were used to fabricate the sensors. The refractive indices of the PDMS and silica were calculated as mentioned before. The RI of the core was determined using the numerical aperture of commercial MMF (105/125) and the assumption that the relative RI difference between the core and the cladding is less than 1 % (for weakly guiding approximation) [27, 28]. The MZI fabricated with a HCF length of 1 mm was simulated at maximum (at 1566.36 nm), and minimum (at 1571.46 nm) transmission, and the result is shown in Fig. 7. The wavelengths used in the simulations were extracted from Fig. 4; it means that experimental data were used in the simulation to observe the different electric field distribution along with the sensor. It can be noticed from the simulations presented in Fig. 7 that, in both cases, when light from the lead-in SMF enters to the MMF, due to the circular symmetric of the fundamental mode of the SMF only the LP_{0m} modes can be excited [29, 30], and thus the MMF works as a beam splitter. When light starts travelling in the HCF, part of the light propagates in the central hole (air), and the remaining propagates in the ring-cladding, which effectively induces an optical path difference between the guided modes allowed to exist in these regions. There is a significant difference in the HCF of these two simulations, the maximum transmission shows more confined light, whereas at minimum transmission exhibits beams of light leaving the HCF. The next section of MMF recombines these modes and creates an interference signal at the lead-out SMF. At the output of both simulations, it is easy to observe that the maximum transmission carries more light in the SMF than the minimum. Then, using the experimental wavelengths as well as the ERI of the modes, we show that the device works as a MZI where two predominant modes interfere.

One application for this MZI is as a bending sensor since the core mode and the cladding mode will experiment different bending losses at different curvatures. At zero curvature, the intensities of each mode determine the contrast of the interference pattern, according to the visibility $V = (I_{\max} - I_{\min}) / (I_{\max} + I_{\min})$. These intensities depend on the alignment of the optical fiber and the losses due to the splicing technique. When the sensor is bent, each mode undergoes different bending losses causing that their intensities vary at the output. These changes in the intensities of each mode modify the visibility and this produce a variation in the contrast of the output signal. As the curvature increase, the bending losses rise for each mode, causing that the intensity of each mode decrease, producing a change in the contrast of the interferometric pattern. In this device can be used to measure curvature using the contrast of the interferometric pattern. In this paper, we present the results obtained when the device was used as a bending sensor.

III. EXPERIMENTAL RESULTS

The bending properties of the fiber MZIs were investigated using the experimental setup shown in Fig. 8 (a). Lead-in SMF was used to launch light into the fiber optic device from a SLD (Superluminescent Diode), and the lead-out SMF collected the output signal and measured it with an OSA (wavelength resolution of 0.02 nm). The ends of the steel sheet were set into the square groove, see 8 (b). The thickness of the steel sheet was 0.7 mm, whereas the square groove thickness was 1.1 mm. This allows that the steel sheet can move along z-axis freely. These metallic pieces were mounted in a rotatory system that was fixed at the top of aluminum posts, see Fig. 8 (c). A sharp metal tube, positioned on the rear part, was used to push the metal sheet to change the curvature from 0 m^{-1} to 2.94 m^{-1} . The small area of the metal tube was glued to the steel sheet to be sure that we are pushing at the same area. The sensor's curvature can be written as

$$C = \frac{1}{R} = \frac{2d}{d^2 + s^2}, \quad (3)$$

where C , R , d , and s are the curvature, the curvature radius, the bending displacement (controlled by the translation state), and the half distance between the edges of the two square grooves, respectively, see Fig. 8 (b).

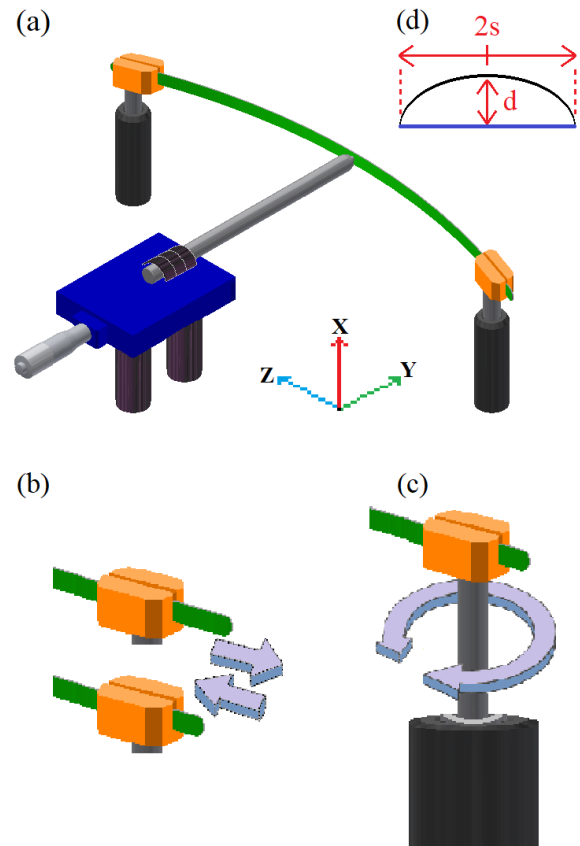
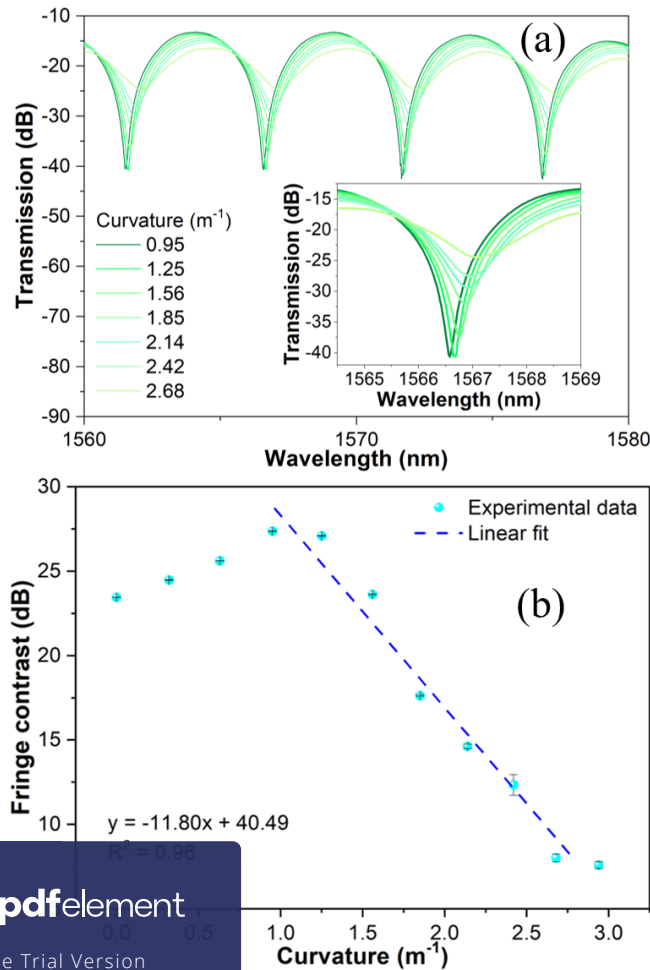


Fig. 8. (a) Experimental setup for curve measurement, (b) Square groove, (c) Rotary system around x-axis, (d) Schematic diagram of the bending setup.

The six MZIs were characterized using the experimental setup shown in Fig. 8 (a). It was observed that the fringe contrast of the interferometric spectrum varies as the sensor curvature changes, and this behavior was present in all MZIs that were implemented. Table 1. shows the sensitivity of the sensors and its associated error, the bending range, and the R-squared. The experiment was conducted three times for each sensor.

Table 1. Experimental sensitivities of the MZIs constructed with different HCF lengths.

L (mm)	Bending sensitivity (dB/m ⁻¹)	Bending range (m ⁻¹)	R-Square
0.5	-8.19 ± 0.45	From 1.56 to 2.94 (1.38)	0.96
1	-11.80 ± 1.30	From 0.95 to 2.68 (1.73)	0.96
1.5	-7.31 ± 0.30	From 0.00 to 2.68 (2.68)	0.99
2	-16.23 ± 2.00	From 2.14 to 2.94 (0.80)	0.97
2.5	-17.28 ± 2.30	From 1.84 to 2.94 (1.10)	0.95
3	-11.41 ± 0.25	From 0.95 to 2.42 (1.47)	0.97



The 2.5 mm long HCF sensor has the highest curvature sensitivity (-17.28 ± 2.30 dB/m⁻¹), whereas the 1 mm long HCF sensor has the most extensive curvature range (from 0.95 m⁻¹ to 2.68 m⁻¹). Since the sensor fabricated with 1 mm of HCF displayed the best performance (sensitivity and curvature range); in the following paragraphs a detailed characterization of this device will be presented. The output signal of the 1 mm long HCF sensor was recorded for different curvatures (from 0 m⁻¹ to 2.94 m⁻¹), as shown in Fig. 9 (a). The maximum curvature value that can be measured, using this system, is limited to the maximum bending displacement ($d = 5$ cm) of the stage, this translation corresponds to a curvature of 2.94 m⁻¹. As the translation stage screw was moving the sensor experimented different curvatures, we used steps of 0.5 cm that correspond to the curvature value of 0.32 m⁻¹.

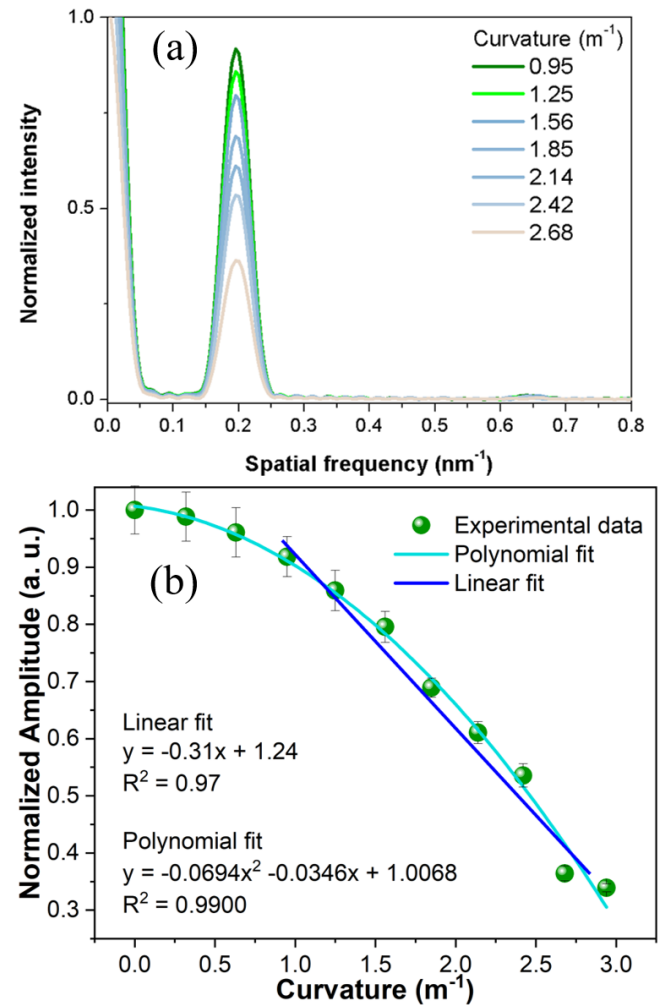


Fig. 10. (a) Calculated FFT of the spectra shown in Fig. 9(a), (b) Normalized amplitude of the FFT as a function of curvature.

We can observe that the amplitude of the signal changed at different curvatures, and one way to quantize this variation is by tracking the fringe contrast of the interference pattern around 1570 nm, see Fig 9. (b). The fringe contrast at 0 m⁻¹ is 22.51 dB, while as the curvature increases until 0.95 m⁻¹, the fringe contrast is increased to 29.32 dB. After this value, the contrast decreases until it reaches a minimum value of 7.72 dB. It can be observed from Fig. 9 (b) that there is a

linear relationship between curvature and fringe contrast, and this linear response occurs in the curvature range that starts from 0.95 m^{-1} to 2.68 m^{-1} with a curvature sensitivity of $-11.80 \pm 1.30 \text{ dB/m}^{-1}$. The main issue in Fig. 9 (b) is that a fitting curve cannot be applied to the whole sensing range.

A better way to monitor the fringe contrast variation is by applying the FFT to the interference pattern, see Fig. 10 (a). For visualization purposes, only the linear region is plotted. It is evident that the data trace has a second-grade polynomial fit, but a linear relationship between the peak amplitude of the FFT and the curvature can be established in the range from 0.95 m^{-1} to 2.68 m^{-1} , see Fig. 10 (b). Its sensitivity was $0.31 \pm 0.02 \text{ a.u.}$. Besides, by using FFT, the curvature measurement range increase (from 0 m^{-1} to 2.94 m^{-1}); in this case, the relationship is a nonlinear expression.

The sensor was set on a hotplate (at curvature 0 m^{-1}) to investigate its temperature response. The spectrum underwent a redshift as the temperature is increased from 30°C to 90°C , as shown in the insert graphs of Fig. 11. Considering that in our case, either the fringe contrast or the amplitude of the FFT is detected, a wavelength-shift does not affect the measurement. The fringe contrast variation as a function of the temperature increment was determined, and its temperature sensitivity was $0.015 \pm 0.007 \text{ dB/m}^{-1}$, see Fig. 11. On the other hand, the peak amplitude of the Fourier spectrum remains almost constant while the temperature was increased ($8.642 \times 10^{-4} \pm 4.525 \times 10^{-5} \text{ a.u.}$), see Fig. 12. The change in the fringe contrast or the peak amplitude of the Fourier spectrum due to temperature is minimal compared to the curvature sensitivity (-11.80 dB/m^{-1} or 0.31 a.u.) and could be neglected when we perform curvature measurements.

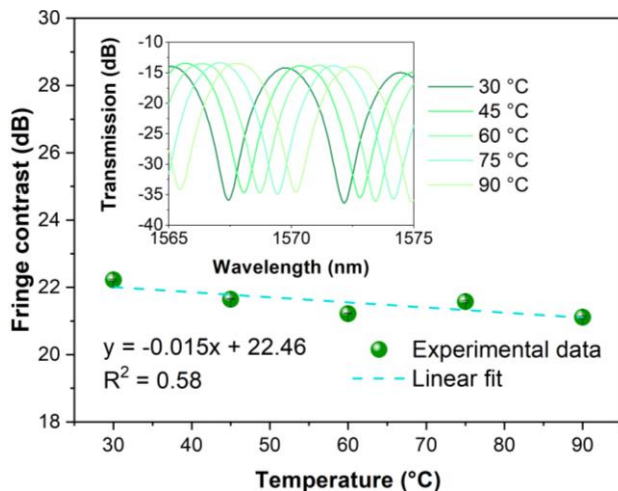


Fig. 11 Fringe contrast as a function of temperature, the insert shows the detailed spectra of the device.

different stages, the sensor was in the middle of the section between this two points. One of these stages was a translation stage that could make small displacement causing strain on the sensor. Fig. 13 shows the spectra of the sensor at different strains; a redshift is observed, but it does not affect the measurement as it was said before. The fringe contrast variation as a function of the strain increment was determined, and its strain sensitivity was $-2.07 \times 10^{-3} \text{ dB/}\mu\epsilon$, see Fig. 13. This means that the fringe contrast variation due to strain is three orders of magnitude lower than the error associated with curvature measurement (1.30 dB/m^{-1}). Consequently, the error produced by the strain during the perform of curvature measurements could be disregard. This makes our sensor sturdier to real applications.

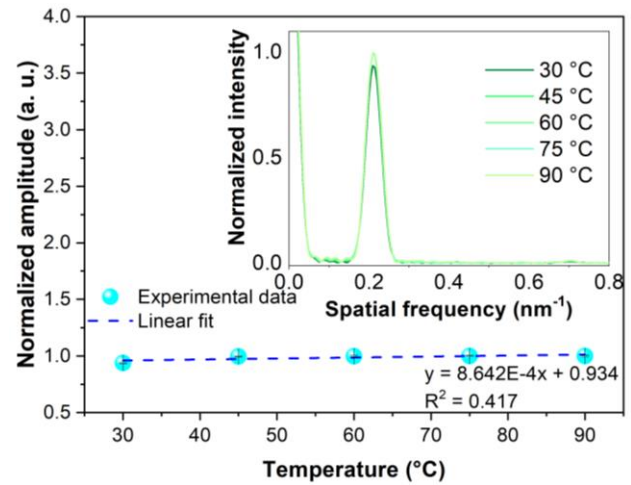


Fig. 12 Normalized amplitude of the FFT as a function of temperature, the insert shows the calculated FFT of the insert shown in Fig. 11.

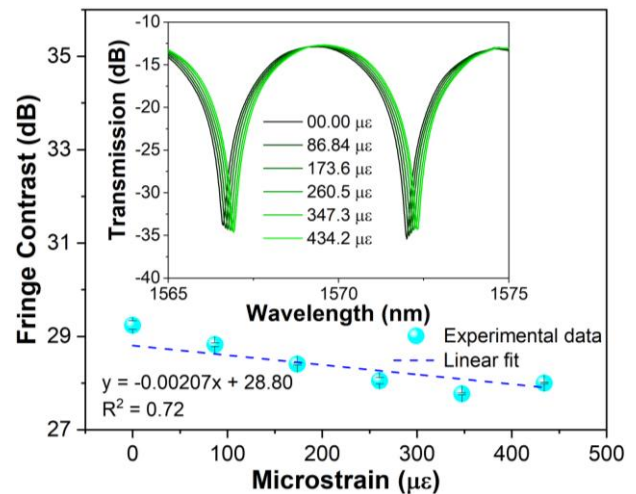


Fig. 13 Fringe contrast as a function of strain, the insert shows the detailed spectra of the device.

IV. CONCLUSION

In summary, we have proposed and experimentally demonstrated an in-fiber MZI to measure bending deformation. The MZI is based on a section of HCF spliced between two sections of MMF. By using the PDMS polymer, the sensor was attached to a steel sheet not only to have a better control of the sensor curvature but also to implement

a sensor packaging for real application in the structural health monitoring. The output signal of the sensor did not undergo significant changes due to the PDMS polymer. Due to the simple fabrication of the device, different lengths of HCF were tested, and all of them work as a curvature sensor. The highest curvature sensitivity was $-17.28 \pm 2.30 \text{ dB/m}^{-1}$ at a curvature range from 1.84 m^{-1} to 2.94 m^{-1} ; the length of the HCF was 2.5 mm. The sensor that demonstrated the best performance was fabricated with a HCF length of 1 mm since it combined good curvature sensitivity ($-11.80 \pm 1.30 \text{ dB/m}^{-1}$) and wider curvature range (from 0.95 m^{-1} to 2.78 m^{-1}). By acquiring the interferometric signal of this device and employing the FFT, it was found that there prevails a nonlinear relation between the contrast and the curvature. Nonetheless, it allowed us to measure the bending on a broader range (from 0 m^{-1} to 2.94 m^{-1}). Furthermore, it exhibited a low fringe contrast temperature dependency (from 30 to 90 °C), which makes the device practically insensitive to temperate fluctuation.

REFERENCES

- [1] C. E. Domínguez-Flores, D. Monzón-Hernández, J. I. Moreno-Basulto, O. Rodríguez-Quiroz, V. P. Minkovich, D. López-Cortés, I. Hernández-Romano, "Real-time temperature sensor based on in-fiber Fabry-Perot interferometer embedded in a Resin," *J. Lightw. Technol.*, vol. 37, no. 4, pp. 1084-90, Feb 2019.
- [2] Y. Lopez-Dieguez, J. M. Estudillo-Ayala, D. Jauregui-Vazquez, L. A. Herrera-Piada, J. M. Sierra-Hernandez, J. C. Hernandez-Garcia, M. Bienchetti, J. R. Reyes-Ayona, R. Rojas-Laguna, "Tip fiber-optic intermodal interferometer for refractive index sensing," *IEEE Photon. Technol. Lett.*, vol. 30, no. 4, pp. 1125-1130, Feb 2017.
- [3] H. Lin, F. Liu, H. Guo, A. Zhou, Y. Dai, "Ultra-highly sensitive gas pressure sensor based on dual side-hole fiber interferometers with Vernier effect," *Opt. Express*, Vol. 26, no. 22, pp. 28763-72, Oct 2018.
- [4] X. Zhang, C. Liu, J. Liu, J. Yang, "Single modal interference-based fiber-optic sensor for simultaneous measurement of curvature and strain with dual-differential temperature compensation," *IEEE Sensors J.*, vol. 18, no. 20, pp. 8375-80, Oct 2018.
- [5] K. Kliewer, B. Glisic, "A curvature based approach using long-gage fiber optic sensors," In *Procc. Health monitoring of Structural and Biological Systems, Las Vegas, Nevada, USA, 2016*, pp. 980520. *International Society for Optics and Photonics*.
- [6] W. H. Png, H. S. Lin, C. H. Pua, J. H. Lim, S. K. Lim, Y. L. Lee, F. A. Rahman, "Feasibility use of in-line Mach-Zehnder interferometer optical fibre sensor in lightweight foamed concrete structural beam on curvature sensing and crack monitoring," *Struct. Health Monit.*, vol. 17, no. 5, pp. 1277-1288, Sep 2018.
- [7] S. Sareh, Y. Noh, M. Li, T. Ranzani, H. Liu, K. Althoefer, "Macrobend optical sensing for pose measurement in soft robot arms," *Smart Mater. Struct.*, vol. 24, no. 12, pp. 1225024, Nov. 2015.
- [8] Y. Zhang, W. Zhang, Y. Zhang, S. Wang, L. Yu, Y. Yan, "Simultaneous measurement of curvature and temperature based on LP₁₁ mode Bragg grating in seven-core fiber," *Meas. Sci. Technol.*, Vol. 28, no. 5, pp. 055101, Mar 2017.
- [9] P. Saffari, T. Allsop, A. Adebayo, D. Webb, R. Haynes, M. M. Roth, "Long period grating in multicore optical fiber: an ultra-sensitive vector bending sensor for low curvatures," *Opt. Lett.*, vol. 39, no. 12, pp. 3508-3511, Jun 2014.
- [10] Y. Zhao, L. Cai, X. G. Li, "In-fiber modal interferometer for simultaneous measurement of curvature and temperature based on hollow core fiber," *Optics & Laser Technol.*, vol. 92, pp. 138-141, Mar 2017.
- [11] Y. J. Rao, Y. Wu, "All-fiber curvature sensor based on Mach-Zehnder interference," *IEEE Photon. Technol. Lett.*, vol. 23, no. 1, pp. 679-681, Mar 2011.
- [12] F. Q. Li, L. Hu, X. Song, Y. Xin, C. L. Zhao, S. Jin, J. C. Chan, "A hollow core fiber-based intermodal interferometer for measurement of strain and temperature," *IEEE Sensors J.*, vol. 13, no. 9, pp. 3468-71, May 2013.
- [13] Y. Zhang, A. Zhou, B. Qin, Q. Xu, Z. Liu, J. Yang, L. Yuan, "Simultaneous measurement of temperature and curvature based on hollow annular core fiber," *IEEE Photon. Technol. Lett.*, vol. 26, no. 11, pp. 1128-31, Apr 2014.
- [14] K. Ni, T. Li, L. Hu, W. Qian, Q. Zhang, S. Jin, "Temperature-independent curvature sensor based on tapered photonic crystal fiber interferometer," *Opt. Commun.*, vol. 285, no. 24, pp. 5148-50, Nov 2012.
- [15] B. Sun, Y. Huang, S. Liu, C. Wang, J. He, C. Liao, G. Yin, J. Zhao, Y. Liu, J. Tang, J. Zhou, Y. Wang, "Asymmetrical in-fiber Mach-Zehnder interferometer for curvature measurement," *Opt. Express*, vol. 23, no. 11, pp. 14596-602, Jun 2015.
- [16] W. Cui, J. Si, T. Chen, X. Hou, "Compact bending sensor based on a fiber Bragg grating in an abrupt biconical taper," *Opt. Express*, vol. 23, no. 9, pp. 11031-6, May 2015.
- [17] C. Sun, Z. Han, S. Zhang, S. Duan, X. Jin, X. Chen, C. Yao, T. Geng, Z. Zhang, Z. Qu, W. Sun, "A micro MMF layer embedded in LPFG for simultaneous measurement of curvature and temperature," *Optical Fiber Technol.*, vol. 48, pp. 134-7, Mar 2019.
- [18] S. Wang, S. Wang, S. Zhang, M. Feng, S. Wu, R. B. Jin, L. Zhang, P. Lu, "An inline fiber curvature sensor based on anti-resonant reflecting guidance in silica tube," *Optics & Laser Technol.*, vol. 111, pp. 407-10, Apr 2019.
- [19] H. Cheng, S. Wu, Q. Wang, S. Wang, P. Lu, "In-line hybrid fiber sensor for curvature and temperature measurement," *IEEE Photon. J.*, vol. 11, no. 6, pp. 6803311, Oct 2019.
- [20] R. Gao, D. Lu, J. Cheng, Z. M. Qi, "Self-referenced antiresonant reflecting guidance mechanism for directional bending sensing with low temperature and strain crosstalk," *Opt. Express*, vol. 25, no. 15, pp. 18081-91, Jul 2017.
- [21] H. Y. Choi, M. J. Kim, B. H. Lee, "All-fiber Mach-Zehnder type interferometers formed in photonic crystal fiber," *Opt. Express*, vol. 15, no. 9, pp. 5711-20, Apr 2007.
- [22] F. Schneider, J. Draheim, R. Kamberger, U. Wallrabe, "Process and material properties of polydimethylsiloxane (PDMS) for Optical MEMS," *Sensors and Actuators A: Phys.*, vol. 151, no. 2, pp. 95-9, Apr 2009.
- [23] I. H. Malitson, "Interspecimen comparison of the refractive index of fused silica," *J. Opt. Soc. Amer.*, vol. 55, no. 10, pp. 1205-9, 1965.
- [24] C. H. Lai, B. You, J. Y. Lu, T. A. Liu, J. L. Peng, C. K. Sun, H. C. Chang, "Modal characteristics of antiresonant reflecting pipe waveguides for terahertz waveguiding," *Opt. Express*, vol. 18, no. 1, pp. 309-322, Jan 2010.
- [25] Y. Wu, Y. Yang, W. Jin, Y. Shen, S. Jian, "Compact Mach-Zehnder interferometer-based no-core fiber hollow-core fiber no-core fiber structure," *Opt. Eng.*, vol. 56, no. 3, pp. 030501, Mar 2017.
- [26] I. Hernández-Romano, D. Monzón-Hernández, C. Moreno-Hernández, D. Moreno-Hernandez, J. Villatoro, "Highly sensitive temperature sensor based on a polymer-coated microfiber interferometer," *IEEE Photon. Technol. Lett.*, vol. 27, no. 24, pp. 2591-4, Sep 2015.
- [27] Y. Jaluria, "Manufacture of optical fibers: drawing and coating processes," in *Advanced materials processing and manufacturing*, 1st ed., Piscataway, NJ, USA, Springer; 2018, ch. 8, sec. 1, pp. 240.
- [28] D. Gloge, "Weakly guiding fibers," *Appl. Opt.*, vol. 10, no. 10, pp. 2252-8, Oct 1971.
- [29] W. S. Mohammed, A. Mehta, E. G. Johnson, "Wavelength tunable fiber lens based on multimode interference," *J. Lightw. Technol.*, vol. 22, no. 2, pp. 469-477, Feb 2004.
- [30] Q. Wang, G. Farrell, W. Yan, "Investigation on single-mode-multimode-single-mode fiber structure," *J. Lightw. Technol.*, vol. 26, no. 5, pp. 512-9, Mar 2008.